

Electrothermal Control of Graphene Plasmon–Phonon Polaritons

Qiushi Guo, Francisco Guinea, Bingchen Deng, Ibrahim Sarpkaya, Cheng Li, Chen Chen, Xi Ling, Jing Kong, and Fengnian Xia*

Graphene plasmons are known to offer an unprecedented level of confinement and enhancement of electromagnetic field. They are hence amenable to interacting strongly with various other excitations (for example, phonons) in their surroundings and are an ideal platform to study the properties of hybrid optical modes. Conversely, the thermally induced motion of particles and quasiparticles can in turn interact with electronic degrees of freedom in graphene, including the collective plasmon modes via the Coulomb interaction, which opens up new pathways to manipulate and control the behavior of these modes. This study demonstrates tunable electrothermal control of coupling between graphene mid-infrared (mid-IR) plasmons and IR active optical phonons in silicon nitride. This study utilizes graphene nanoribbons functioning as both localized plasmonic resonators and local Joule heaters upon application of an external bias. In the latter role, they achieve up to ≈ 100 K of temperature variation within the device area. This study observes increased modal splitting of two plasmon–phonon polariton hybrid modes with temperature, which is a manifestation of increased plasmon–phonon coupling strength. Additionally, this study also reports on the existence of a thermally excited hybrid plasmon–phonon mode. This work can open the door for future optoelectronic devices such as electrically switchable graphene mid-infrared plasmon sources.

Graphene plasmonic nanostructures exhibit extreme light confinement^[1,2] and strongly enhanced near fields. This enables the plasmonic modes to interact strongly with various excitations in their local environments, such as phonons (lattice vibrations), molecular vibrations, or excitons. These unique properties of the graphene plasmon have far-reaching implications for topics as diverse as enhanced light–matter interaction,^[2,3] ultrasensitive molecular sensing,^[4] and the accessing of various forbidden transition states.^[5] Specifically, experiments performed on graphene devices on polar substrates have shown that the graphene plasmon dispersion relation is strongly modified by the long-range Fröhlich coupling to the substrate surface optical (SO) phonons; these new modes are known as hybrid plasmon–phonon (HPP) modes.^[6–9] As a reverse process of this interaction, one can expect that changes in substrate phonon property will in turn alter the HPP mode properties through strong Coulomb interactions. Recent experiments have shown that thermally excited phonons in the sub-

strate can not only serve as incoherent blackbody emitters but also generate graphene mid-IR plasmons, which subsequently radiate into the free space.^[10] As such, the studies of the actively tunable phonon–plasmon interaction between graphene and the substrate phonons are of substantial interest as it provides routes to tailor or excite plasmons in graphene in addition to optical methods.

In this work, we experimentally demonstrate electrothermal control of coupling between graphene plasmons and surface phonons in silicon nitride substrate. The SO phonons of SiN_x are located at a frequency, which allows them to strongly couple with graphene plasmons at a modest graphene doping level. According to thermal IR emission measurement, we achieved ≈ 100 K of localized temperature increase in the device area by passing a current through graphene nanostructures. It is shown that the plasmon–phonon coupling strength increases as the local temperature rises, which manifests as the increased energy splitting between two plasmon–phonon polariton modes. Polarization-dependent measurements further validate the excitation of the unique HPP modes enabled by the thermally generated phonons in the substrate. This work offers the

Q. Guo, B. Deng, Dr. I. Sarpkaya, C. Li, C. Chen, Prof. F. Xia

Department of Electrical Engineering

Yale University

New Haven, CT 06511, USA

E-mail: fengnian.xia@yale.edu

Prof. F. Guinea

IMDEA Nanociencia

Calle de Faraday 9, E-28049 Madrid, Spain

Prof. F. Guinea

Department of Physics and Astronomy

University of Manchester

Oxford Road, Manchester M13 9PL, UK

Prof. X. Ling

Department of Chemistry

Boston University

Boston, MA 02215, USA

Prof. J. Kong

Department of Electrical Engineering and Computer Science

Massachusetts Institute of Technology

Cambridge, MA 02139, USA

DOI: 10.1002/adma.201700566

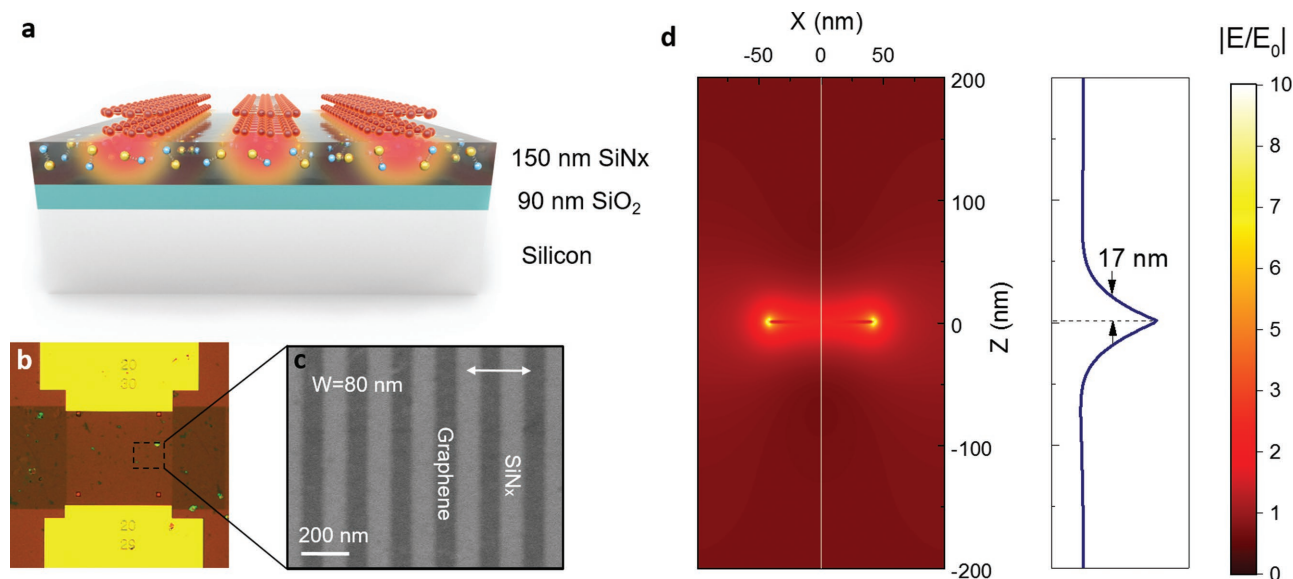


Figure 1. a) Schematic of the experimental device. b) Optical and c) SEM image of graphene nanoribbon array device. In (c) W indicates the graphene ribbon width and the arrow represents the linear polarization direction of the incident IR radiation. d) Mode profile of the graphene plasmonic mode of a 100 nm freestanding graphene nanoribbon with Fermi level of -0.3 eV, obtained from a FDTD simulation. The right panel shows the near-field distribution along the white solid line in the left panel. The field decay length is around 17 nm.

possibility for engineering graphene plasmonic emitters in the infrared via strong plasmon–phonon coupling and future applications such as chip-scale electrothermally generated mid-IR sources.

A schematic image of our experimental device is shown in **Figure 1a**. We first deposited ≈ 150 nm amorphous SiN_x using plasma-enhanced chemical vapor deposition (PECVD) at 400 °C on a SiO₂ (90 nm)/highly resistive silicon substrate. Two monolayer graphene sheets grown using chemical vapor deposition on copper foil were subsequently transferred onto the substrate. The individual graphene sheet transferred by this method is hole-doped with a Fermi level of ≈ -0.3 eV,^[11] corresponding to a carrier density of $6.6 \times 10^{12} \text{ cm}^{-2}$. Nanoribbons were patterned into this resultant double-layer graphene using electron beam lithography and the subsequent oxygen plasma etching. A second lithography process was used to define the electrode pattern. Finally, 8 nm chromium (Cr) and 30 nm gold (Au) were deposited and lift-off in acetone formed the electrodes. The optical image of the resulting device is shown in **Figure 1b**. The use of double-layer graphene allows for stronger graphene plasmonic resonances at mid-infrared frequencies.^[12] Moreover, the highly conductive graphene ribbons can also serve as efficient Joule heaters at fixed voltage bias. In order to enable the Joule heating, the graphene ribbons are electronically continuous with a 1:2 width-to-pitch ratio, as shown in the scanning electron microscopy (SEM) image in **Figure 1c**. One of the most remarkable features of the graphene plasmon is its strong electric field confinement. In **Figure 1d**, we provide the simulated near-field distribution of a freestanding 100 nm wide double-layer graphene nanoribbon at its fundamental plasmonic resonance. The electric field is tightly confined near the graphene nanoribbons with a field decay length only about 17 nm. Therefore, the graphene plasmon will only interact with the underlying SiN_x substrate but not with SiO₂.

To investigate absorption resonances arising from mid-IR graphene plasmons, an infrared microscope coupled to a Fourier-transform infrared spectrometer (FTIR) was used to measure the mid-infrared transmission spectra of these graphene nanoribbon arrays. The transmission extinction ($1 - T/T_0$) was used to characterize the infrared optical responses,^[12] where T is the transmission of the light through the ribbon array and the substrate, T_0 is the transmission through only the substrate.^[12] The incident light was polarized perpendicular to graphene nanoribbons in order to effectively excite the plasmons. When the incident light is coupled to a graphene plasmon mode with the wave vector k_p , the plasmon undergoes multiple reflections between the two edges of the nanoribbon. Constructive interference occurs when the reflected plasmons are in phase, which occurs when $2\text{Re}\{k_p\}W + 2\phi = 2m\pi$, where W is the width of the nanoribbon, $m = 1, 2, 3, \dots$ and ϕ is the phase shift of the plasmons upon reflection. It should be noted that only plasmonic modes with odd multiples of half-wavelengths ($m = \text{odd number}$) can produce an effective net charge dipole that creates the necessary restoring force for collective charge oscillations.^[13] When graphene is resting on a polar substrate such as SiN_x, which accommodates surface optical (SO) phonons,^[14] the long-range electric fields generated by optically active phonon modes in the substrate can significantly alter the collective plasmonic mode in graphene. **Figure 2a** presents extinction spectra for double-layer graphene ribbons on a SiN_x substrate with ribbon width (W) ranging from 60 to 200 nm, revealing two prominent resonance peaks within our measured frequency range of interest ($600\text{--}3500 \text{ cm}^{-1}$) instead of a single plasmonic mode. In fact, the ion oscillations in the SiN_x give rise to a sharp increase in the SiN_x dielectric constant below its phonon energy. Since the graphene plasmon wavelength (λ_p) depends strongly on the surrounding dielectric media, the high dielectric constant of the SiN_x around its phonon

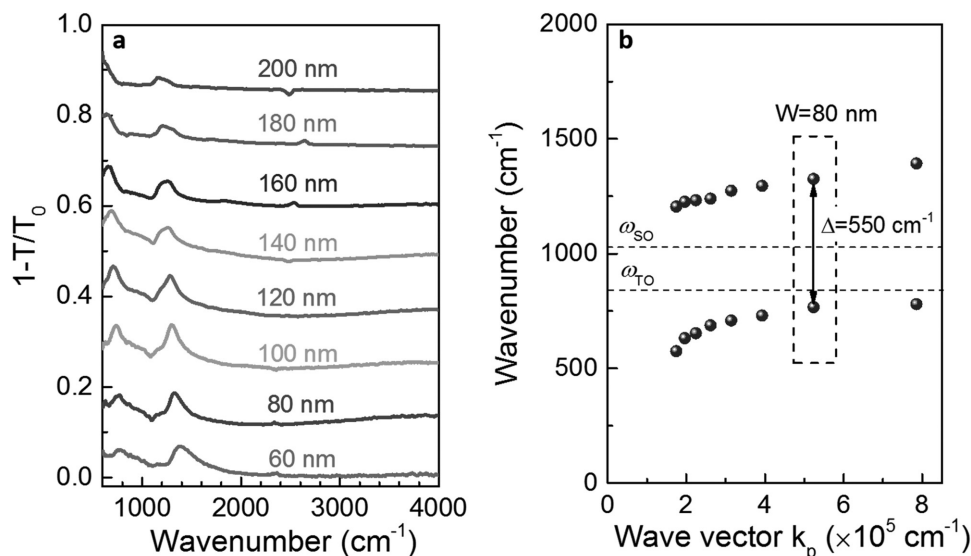


Figure 2. a) Infrared extinction spectra of double-layer graphene nanoribbon arrays on 150 nm SiN_x. The incident light is always polarized perpendicular to the ribbons. W varies from 60 to 200 nm. Spectra are shifted vertically by 12% consecutively for clarity. b) Plasmon frequency as a function of wave vector $k_p = \pi/W_e$ for peaks shown in (a). The SiN_x TO and SO phonon frequencies are labeled by dashed lines.

frequency further compresses graphene plasmons in space, allowing the graphene nanoribbons to support additional low energy plasmon oscillations. Thus these two modes represent composite excitations consisting of plasmons in the graphene coupled to phonons in the SiN_x, which are hence known as surface HPP modes.^[8] In addition, it can be seen from Figure 2a that the resonant frequencies of extinction peaks blue-shift as W decreases since smaller resonator requires shorter λ_p to satisfy the standing wave condition. Here, we want to clarify that due to the strong confinement of graphene plasmon with field decay length on the order of tens of nanometers,^[8] the coupling between graphene plasmon and the SiO₂ optical phonon is negligible in the current device architecture. Figure 2b depicts the dependence of the resonance peak frequencies obtained from the spectra in Figure 2a. We defined the wave vector of the localized plasmon to be $k_p = \pi/(W - W_0)$. Here $W_e = W - W_0$ denotes the effective ribbon in which W is the ribbon's actual physical width and W_0 (about 20 nm in this work) accounts for defects and edge chemistry caused by the fabrication process.^[11] It can be found that when $W = 80$ nm, the two HPP modes have minimal splitting of 550 cm⁻¹. The TO and SO phonon frequencies of the SiN_x substrate are also labeled in Figure 2b. With $W = 80$ nm, the SO phonon frequencies lies in the middle of the two HPP modes frequencies.

When a sizable current is passed through the graphene, the electronic energy can be transformed into heat via Joule heating. This heat then diffuses into both the SiN_x and SiO₂ layers. The SiO₂ layer has a lower thermal conductivity (≈ 1.4 W m⁻¹ K⁻¹) so it inhibits the heat transfer from the SiN_x to the silicon substrate which has high thermal conductivity (≈ 149 W m⁻¹ K⁻¹) and acts as a heat sink. Simultaneously, a small fraction of heat is radiated into free space, which can be detected spectrally in the mid-IR or near-IR by observing its thermal emission. Bias-dependent emission spectra were recorded using a FTIR microscope. The emitted light from the heated device was collected by a Cassegrain objective, then collimated and passed through

the interferometer in the FTIR before being focused on a liquid nitrogen-cooled HgCdTe (MCT) detector. Note that by monitoring the real-time emission spectra with bias, we found that ≈ 30 s is enough for the entire system to reach thermal equilibrium. Therefore in all the following measurements with Joule heating, a voltage biasing time of 30 s was employed before collecting spectral data. As shown in Figure 3a, we obtained the current–voltage relationship for the Joule heating scheme, from which a 1.4 k Ω device resistance was derived. Figure 3b shows four sets of infrared emission spectra at different bias conditions, fitted to the Planck's law modified with an emissivity ϵ

$$u(\nu, T) = \epsilon \frac{8\pi}{h^2 c^3} \frac{(h\nu)^3}{\exp(h\nu/k_B T) - 1} \quad (1)$$

where u is the spectra energy density, k_B is the Boltzmann constant, $h\nu$ is the photon energy, and T is the temperature of graphene. We discarded the thermal emission spectra below 2200 cm⁻¹, which contain background noise from the environment. We determined both ϵ and T by fitting the emission spectra using Equation (1). We find T ranges from 317 K at 20 V bias to 410 K at 50 V bias. This indicates that the Joule heating can result in approximately 100 K local temperature increase.

Because the occupancy of the optical phonons rises with elevated temperature, this leads to an increase in the number of phonons within a volume and in turn, the phonon oscillator strength and the electron–phonon coupling strength.^[15] A Lorentz oscillator model with N modes is used to model the dielectric function of the SiN_x substrate

$$\epsilon_{\text{subs.}}(\omega) = \epsilon_\infty + \sum_{j=1}^N f_j \frac{\omega_{\text{TO},j}^2}{\omega_{\text{TO},j}^2 - \omega^2 - i\omega\Gamma_{\text{TO},j}} \quad (2)$$

where ϵ_∞ denotes the high-frequency dielectric constant of the polar substrate and $\omega_{\text{TO},j}$ corresponds to the frequency of the material's j -th bulk transverse optical (TO) phonon mode. The

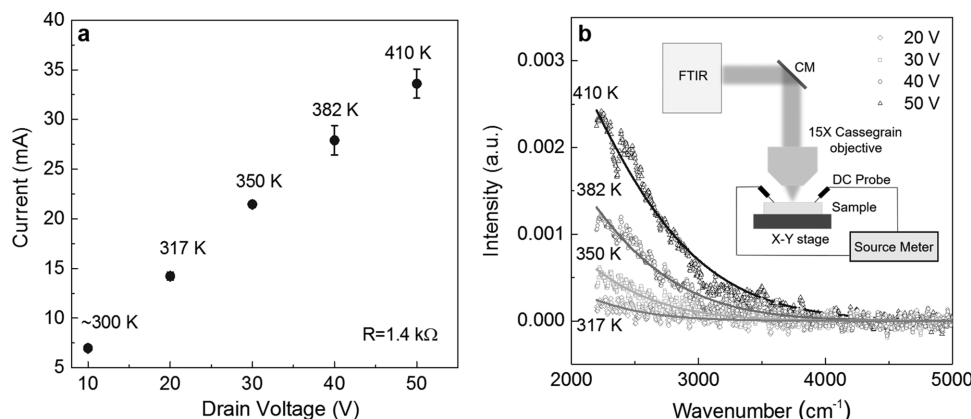


Figure 3. a) Current–voltage characteristic of 100 $\mu\text{m} \times 100 \mu\text{m}$ graphene nanoribbon array with 80 nm ribbon width. The error bars account for the current fluctuations in the measurements. At different bias voltages, the corresponding local temperatures obtained from the infrared emission measurements are labeled in the figure. b) Measured infrared emission from biased graphene for four different bias conditions as indicated. Solid lines are fits to Equation (1). Inset: experimental set-up consisting of a probe station mounted on the x–y sample stage, FTIR with an MCT detector inside. CM: coupling mirror.

dimensionless quantity denoted by f_j characterizes the oscillator strength, i.e., it gauges the relative contribution of each mode to the total screening properties of the substrate, and it satisfies the sum rule $\sum_{j=1}^N f_j = \epsilon_s - \epsilon_\infty$,^[16] where ϵ_s is the static dielectric constant. The oscillator strength of j -th mode is $f_j = \epsilon_{(j-1)} - \epsilon_{(j)}$,^[17] with $\epsilon_{(0)} \equiv \epsilon_s$ being the static dielectric constant and $\epsilon_{(N)} \equiv \epsilon_\infty$ being the high frequency dielectric constant. $\epsilon_{(j-1)}$ and $\epsilon_{(j)}$ denote the dielectric constant at the frequency lower and higher than the oscillation frequency of j -th mode, respectively. The frequencies (ω_{sp}) corresponding to the surface optical (SO) phonons (Fuchs–Kliwer excitations) at the interface can be determined from $\epsilon_{\text{subs.}}(\omega) + 1 = 0$.^[18] Here we assume $\omega_{\text{TO},j}$ is the frequency of the SiN_x TO phonon mode discussed in this work and f_j is its modal oscillator strength. Within the framework of random phase approximation, the biquadratic equation with coupled plasmon–phonon modes solutions is given by^[11]

$$\omega_{p\pm}^2(k) = \frac{\omega_{sp}^2 + \omega_p^2}{2} \pm \frac{\sqrt{(\omega_{sp}^2 + \omega_p^2)^2 - 4\omega_p^2(\omega_{sp}^2 - \tilde{\omega}_{sp}^2)}}{2} \quad (3)$$

where $\omega_{sp}(k)$ is the surface optical phonon frequency and $\omega_p(k)$ is the graphene plasmon mode frequency. The two branches $\omega_{p\pm}(k)$ describe the dispersion relations of two HPP modes involving both collective electronic and ion oscillations.

$\tilde{\omega}_{sp}^2 = \sqrt{\frac{4\pi}{\hbar} \omega_{sp} F^2}$, where $F^2 = \frac{\hbar \omega_{sp}}{2\pi} \left(\frac{1}{\epsilon_{(j)} + \epsilon_{\text{env}}} - \frac{1}{\epsilon_{(j-1)} + \epsilon_{\text{env}}} \right)$ describes the Fröhlich coupling strength between the electrons in graphene and j -th phonon mode and ϵ_{env} is the dielectric constant of the environment. It can be shown that the minimum modal splitting

$$\Delta = (\omega_+ - \omega_-) \propto \omega_{sp} \sqrt{f_j} \quad (4)$$

which occurs at $\omega_{sp} = \omega_p$ (see Supporting Information). In fact, there are two competing mechanisms for the thermal tuning of HPP modes. Due to the anharmonic contributions to the interatomic potential energy,^[19] the surface optical phonon frequency (ω_{sp}) of the SiN_x can decrease at higher temperatures.

A theoretical model which accounts for this effect is discussed in the supporting information. However, the more significant increase of phonon oscillator strength f_j at elevated temperature would compensate the reduction in ω_{sp} and finally give rise to increased modal splitting Δ .

In Figure 2b, we have shown that when $W = 80 \text{ nm}$, graphene plasmon frequency ω_p is geometrically tuned to coincide with SiN_x surface optical phonon frequency ω_{sp} provided that the splitting between two HPP modes is minimal. Figure 4a presents the extinction spectra ($1 - T/T_0$) of 80 nm graphene nanoribbon under different biases. In all measurements, the transmission references (T_0) were measured on the bare SiN_x substrate only without bias (room temperature). One can see that the energy splitting between the two plasmon–phonon polariton peaks increases from 550 to 655 cm^{-1} as the phonon density in the SiN_x gradually increases due to the Joule heating induced by the voltage bias. Besides the change in the energy splitting, an enhancement of the lower frequency hybrid mode extinction was also observed, with intensity increased from 5% to 11%. We attribute this to the increase in the TO phonon oscillating strength and corresponding absorption coefficient while the SiN_x is heated.

To further quantify the change of the phonon oscillator strength in response to the Joule heating, we employed a finite-difference time-domain (FDTD) model to simulate the optical properties of the device. The details of this modeling process are described in the Experimental section. The black dots in the inset of Figure 4b depict the measured absolute reflection spectra of 150 nm $\text{SiN}_x/90 \text{ nm SiO}_2/\text{Silicon}$ substrate referenced to a gold mirror. Two reflection peaks are found at 848 cm^{-1} and 1083 cm^{-1} which result from the TO phonons of SiN_x and SiO_2 , respectively. We then incorporated the Lorentz oscillator model (Equation (2)) into our FDTD simulation in order to model the SiN_x dielectric response. The standard SiO_2 dielectric function was adopted from ref. [5]. The best fit to the experimental data is depicted as a red line in inset of Figure 4b. It is seen that they are in good agreement, which validates our model. From the fitting, we obtained the SiN_x parameters $\epsilon_\infty = 4.2$, $\Gamma_{\text{TO},j} = 165.7 \text{ cm}^{-1}$ and the oscillator strength

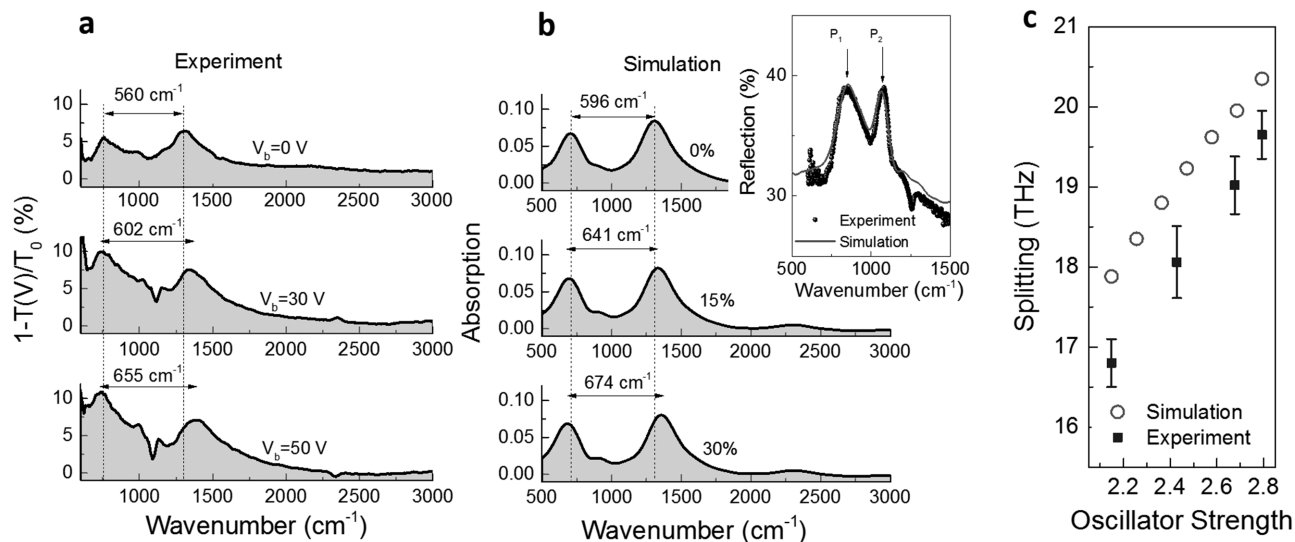


Figure 4. a) Experimental IR extinction spectra of 80 nm graphene nanoribbon arrays under various source–drain biases. The incident light is always polarized perpendicular to the ribbons. T_0 denotes the transmission measured at the bare SiN_x substrate with zero bias. b) Simulated infrared absorption spectra of double-layer graphene nanoribbon arrays on SiN_x with various SiN_x phonon oscillator strengths (increased by 15% for each panel). Inset: comparison between experimental (black dots) and simulated (solid line) IR reflection spectra of SiN_x . P_1 (P_2) corresponds to reflection peak result from SiN_x (SiO_2) phonon. c) Dependence of experimental (square dots) and simulated (circles) minimal modal frequency splitting on SiN_x phonon oscillator strength. The error bars quantify the uncertainties in determining the peak frequencies.

$f_j = 2.12$. With these fitting parameters, we plotted the simulated IR absorption spectra of double-layer graphene ribbons in the presence of substrate phonons in Figure 4b. In the simulation, the doping level of each graphene layer was set to be 0.3 eV and a realistic carrier mobility of $600 \text{ cm}^2 \text{ V}^{-1} \text{ s}^{-1}$ was assumed, which are estimated using previous transport measurement results from similar wafers. With zero percentage change in f_j (at room temperature with zero bias), the simulated Δ is 595 cm^{-1} , slightly greater than the experimental value (550 cm^{-1}), which can be attributed to the graphene wrinkles^[20] or other nonidealities associated with the graphene/ SiN_x interface in the experimental device.^[9,21] Similar to what we have observed experimentally, the simulated modal splitting becomes larger as f_j increases ($\approx 80 \text{ cm}^{-1}$ if f_j is set to increase by 30%). It ought to be noted that the simulated spectra shown in Figure 4b only contain the absorption information of double-layer graphene, they do not account for experimentally increased phonon absorption in SiN_x at elevated temperature as shown in Figure 4a. However, the simulated IR extinction spectra (see the Supporting Information) can capture this phenomenon, although the Lorentz oscillator model does not account for the lowering of SiN_x TO phonon frequency at higher temperatures. The temperature increase at the SiN_x surface will cause heat diffusion and an increase of the underneath SiO_2 layer. In Figure 4a, the dispersive feature at 1100 cm^{-1} originates from the increase of SiO_2 TO phonon oscillation strength as well as the blue-shift (anharmonicity) of this phonon mode after the Joule heating. Furthermore, we have also estimated the percentage change of the f_j in response to the Joule heating by comparing the experimental extinction spectra with simulated extinction spectra (see the Supporting Information). Figure 4c summarizes the dependency of experimental and simulated Δ on the phonon oscillator strength f_j .

In addition to the tuning of plasmon–phonon coupling strength discussed above, the enhanced TO and corresponding SO local phonon density enabled by the Joule heating will also induce collective carrier oscillations in graphene, which can be regarded as thermally generated HPP modes. This is a direct consequence of electron–phonon interaction resulting from the Coulomb potential,^[21] such that electron–hole (e – h) dipole moments in graphene are induced by the SO phonons. Since the HPP mode excitation manifests itself as enhanced light absorption, we investigated the thermally generated HPP mode by monitoring extinction spectra at the graphene ribbon region with Joule heating. Simply put, here we employed the IR radiation to detect the thermally generated HPP modes. Figure 5a depicts the evolution of normalized transmission spectra $[T_{\text{per}}(V)/T_{\text{per}}(0)]$ of 80 nm graphene nanoribbon array at various biases. All transmission spectra were referenced to the transmission measured at zero bias (room temperature) with polarization perpendicular to the ribbons $[T_{\text{per}}(0)]$. With zero voltage bias, $T_{\text{per}}(V)/T_{\text{per}}(0)$ is simply unity as can be seen from the Figure 5a leftmost panel. In the presence of Joule heating, additional hybrid plasmon–phonon mode absorption occurs $\approx 1380 \text{ cm}^{-1}$ can be observed (marked by black dots). The absorption becomes more pronounced with increased bias voltage and $\approx 2\%$ was achieved under 50 V bias. Moreover, the peak absorption frequency also increases from 1375 cm^{-1} (at 20 V bias) to 1421 cm^{-1} (at 50 V bias), due to the enhanced phonon–plasmon coupling strength and the subsequently enhanced splitting. Again, the low-frequency absorption feature $\approx 800 \text{ cm}^{-1}$ is mainly ascribed to the enhanced TO phonon absorption of SiN_x at elevated temperatures. It is therefore difficult to conclude the existence of a thermally excited plasmon mode at lower frequencies from this measurement only. As a control experiment, Figure 5b shows the normalized

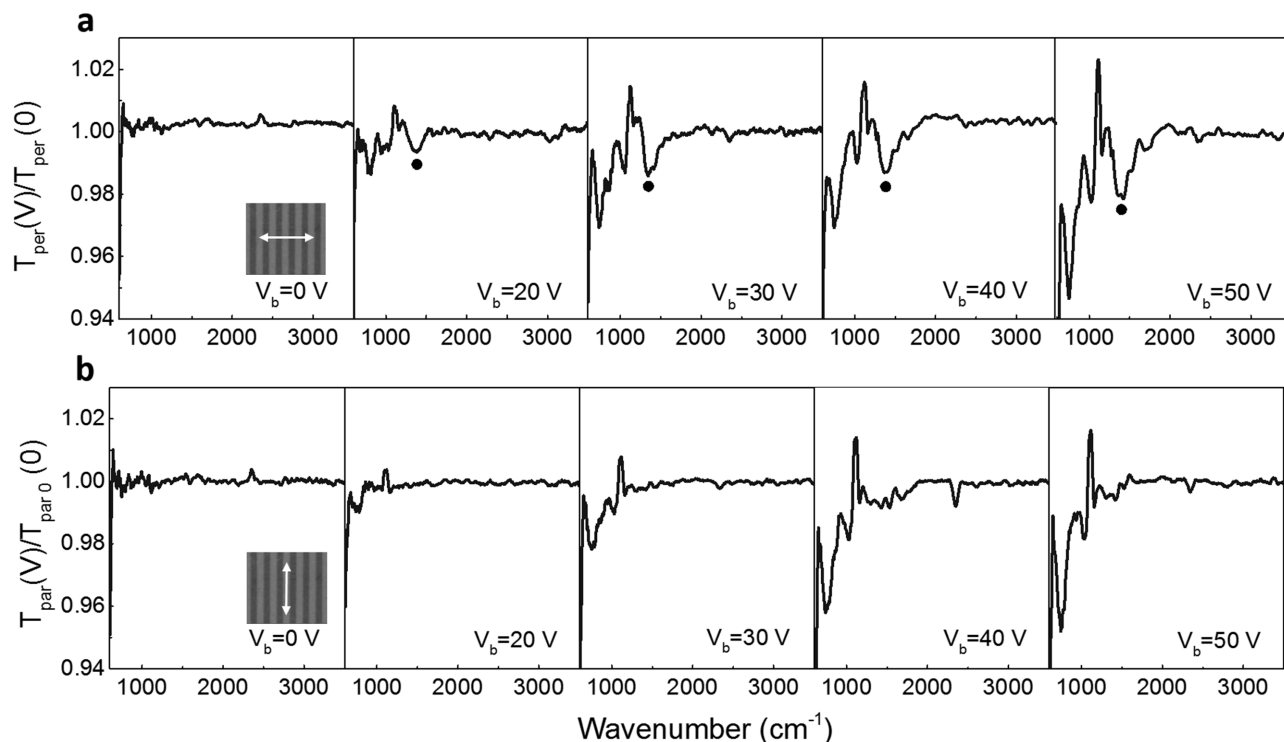


Figure 5. a) Normalized IR transmission spectra of double-layer graphene nanoribbon array on SiN_x under various source-drain biases. The incident light is always polarized perpendicular to the ribbons (inset). The additional hybrid plasmon-phonon modes are labeled by black dots. b) Normalized IR transmission spectra of double-layer graphene nanoribbon arrays on SiN_x under various source-drain biases. The incident light is always polarized in parallel to the ribbons (inset). For both (a) and (b), $W = 80$ nm.

transmission spectra with polarization parallel to the ribbons. All transmission spectra were referenced to the transmission measured at zero bias (room temperature) with polarization in parallel to the ribbons [$T_{\text{par}}(0)$]. In stark contrast to the results shown in Figure 5a, there is no observable absorption feature ≈ 1380 cm^{-1} but enhanced TO phonon absorption at ≈ 800 cm^{-1} is evident. We want to clarify that in Figure 5a,b, the transmission dip (≈ 800 cm^{-1}) corresponding to TO phonon absorption frequency gradually red-shifts at higher temperatures mainly due to phonon anharmonicity. In contrast to the optically excited plasmons whose e - h dipole moments are always in parallel with the incident light polarization direction, thermally generated HPP modes in graphene are randomly oriented, given the disordered nature of the SiN_x phonons. However, by patterning graphene into nanoribbons, the HPP modes density in the direction perpendicular to the ribbon can be significantly higher since spatial confinement enables the constructive interference of HPP waves and the buildup of electromagnetic energy in this direction. In other words, in this direction, there are more e - h dipole moments oscillating around the SiN_x SO phonon frequency, which are able to couple with incident light polarized in this direction. This explains why we only observed the thermally generated HPP modes when the incident light is polarized perpendicular to the ribbons (Figure 5a).

In conclusion, we use a Joule heating scheme to demonstrate the tuning effect of the coupling strength between graphene plasmons and substrate surface optical phonons. As a direct consequence of the strong plasmon-phonon coupling, the thermally excited surface phonons in the SiN_x substrate

can interact with the free electrons in the graphene and lead to hybrid HPP mode excitation, which was further experimentally validated by the resultant enhanced light absorption. More generally, the electrothermal technique presented here can be applied to various crystalline polar substrates, ideally with even lower phonon absorption loss, for example, single crystalline SiC.^[22] With lower phonon absorption loss, the electrothermal modulation depth is expected to be further enhanced. One could also conceivably pattern the polar substrate^[23] in order to boost the local optical phonon density and hence the coupling strength.

On a different front, the utilization of spectrally sharp surface phonon modes of materials such as SiC remains to be a dominant enabling mechanism for chip scale mid-IR thermal emitters.^[24] Nevertheless, these devices are difficult to be miniaturized and usually exhibit narrow-band emissions, which are barely tunable once the structure is fabricated. For some applications, such as chip-scale mid-IR spectroscopy or IR molecular sensing or fingerprinting systems,^[25] integrated mid-IR sources with broader spectral emission are desirable but still less readily available. We envision that our work will not only provide a strategy to realize electrically switchable infrared sources but can also extend the functionalities of existing thermal emitters. In addition, according to Brar et al.,^[8] the mode volume of the hybrid phonon-plasmon modes are even smaller than the pure graphene plasmonic mode. Hence these hybrid modes can be employed to further improve the sensitivity of current graphene plasmonic molecular sensors.^[4,26] As a future perspective, our proposed device platform can function as both IR source and

sensing component, with the molecules induced signal change being detectable by a single mid-IR photodetector. This may greatly simplify the current IR molecular detection and analysis schemes which are heavily relying on bulky and expensive IR spectrometers.

Experimental Section

IR Emission Measurements: The setup consists of a microscope (Bruker Hyperion 2000) that can operate in either spectroscopy or imaging modes and an FTIR (Vertex 70). A homemade probe station was mounted on the microscope sample stage. A source meter (Keithley 2612B) was used to bias the device and collect the current. Infrared radiation emitted by a heated sample is collimated by a Cassegrain objective and guided into an FTIR spectrometer. After passing through a Michelson interferometer, thermal emission was focused by a parabolic mirror and impinged on a liquid nitrogen-cooled HgCdTe detector. For both the IR emission and the IR extinction measurements, data collected were averaged over 64 scans with 4 cm^{-1} spectral resolution.

Electromagnetic Simulations: The optical response of graphene/SiN_x system was simulated using Lumerical FDTD Solutions (2016a). A graphene layer was modeled using a uniaxial anisotropic permittivity assuming that the graphene layer has a finite thickness (C (graphene)-Falkovsky (mid-IR) material model). In the model, graphene's conductivity is described by a Drude-like expression which is valid for mid-infrared wavelengths, since in the mid-infrared, the intraband conductivity term usually dominates over the interband term. A 3D model was constructed by specifying the width, thickness, periodicity of the graphene nanoribbons array. Periodic boundary conditions were imposed on two sides and absorption boundary conditions (PML) were imposed both on the top and the bottom of the simulation region. A plane wave source of appropriate bandwidth ($500\text{--}3000\text{ cm}^{-1}$) was launched toward the top of the graphene, and linear monitors were placed to collect the total reflectance/transmittance as a function of wavelength. In order to reduce the simulation time consumption, we set the single graphene layer to be 1 nm in thickness and the corresponding permittivity of graphene was normalized to match the thickness of 1 nm. The mesh size of our simulation was set to be 0.5 nm due to limited computational power and the thickness of the double-layer graphene ribbon was set to 2 nm. During the meshing process, we further verified that the transmission or reflection spectrum did not change with the denser mesh. The Fermi level of each graphene layer was set to be -0.3 eV and a mobility of $600\text{ cm}^2\text{ V}^{-1}\text{ s}^{-1}$ was assumed for each layer in order to match the experimental conditions. The absorption from the double-layer graphene was calculated by calculating the volumetric integral of electromagnetic power absorbed by graphene normalized to the total incident light power.

Supporting Information

Supporting Information is available from the Wiley Online Library or from the author.

Acknowledgements

The authors thank the National Science Foundation CAREER Award (ECCS 1552461) and the Office of Naval Research (N000141410565) for the support of this work. F.G. was supported by funding from the European Union through the ERC Advanced Grant NOVGGRAPHENE through grant agreement Nr. 290846, and from the European Commission under the Graphene Flagship, contract CNECTICT-604391.

Conflict of Interest

The authors declare no conflict of interest.

Keywords

graphene mid-IR plasmon, hybrid plasmon-phonon modes, Joule heating

Received: January 27, 2017

Revised: April 5, 2017

Published online: June 16, 2017

- [1] a) Z. Fei, A. Rodin, G. Andreev, W. Bao, A. McLeod, M. Wagner, L. Zhang, Z. Zhao, M. Thiemens, G. Dominguez, *Nature* **2012**, *487*, 82; b) J. Chen, M. Badioli, P. Alonso-González, S. Thongrattanasiri, F. Huth, J. Osmond, M. Spasenović, A. Centeno, A. Pesquera, P. Godignon, *Nature* **2012**, *487*, 77.
- [2] F. H. Koppens, D. E. Chang, F. J. G. de Abajo, *Nano Lett.* **2011**, *11*, 3370.
- [3] B. Deng, Q. Guo, C. Li, H. Wang, X. Ling, D. B. Farmer, S.-J. Han, J. Kong, F. Xia, *ACS Nano* **2016**, *10*, 11172.
- [4] a) D. Rodrigo, O. Limaj, D. Janner, D. Etezadi, F. J. G. de Abajo, V. Pruneri, H. Altug, *Science* **2015**, *349*, 165; b) Y. Li, H. Yan, D. B. Farmer, X. Meng, W. Zhu, R. M. Osgood, T. F. Heinz, P. Avouris, *Nano Lett.* **2014**, *14*, 1573; c) F. Liu, E. Cubukcu, *Phys. Rev. B* **2013**, *88*, 115439.
- [5] N. Rivera, I. Kaminer, B. Zhen, J. D. Joannopoulos, M. Soljačić, *Science* **2016**, *353*, 263.
- [6] a) A. Woessner, M. B. Lundberg, Y. Gao, A. Principi, P. Alonso-González, M. Carrega, K. Watanabe, T. Taniguchi, G. Vignale, M. Polini, *Nat. Mater.* **2015**, *14*, 421; b) I. J. Luxmoore, C. H. Gan, P. Q. Liu, F. Valmorra, P. Li, J. R. M. Faist, G. R. Nash, *ACS Photonics* **2014**, *1*, 1151; c) Y. Jia, H. Zhao, Q. Guo, X. Wang, H. Wang, F. Xia, *ACS Photonics* **2015**, *2*, 907; d) Z. Fei, G. O. Andreev, W. Bao, L. M. Zhang, A. S. McLeod, C. Wang, M. K. Stewart, Z. Zhao, G. Dominguez, M. Thiemens, *Nano Lett.* **2011**, *11*, 4701.
- [7] V. W. Brar, M. S. Jang, M. Sherrott, J. J. Lopez, H. A. Atwater, *Nano Lett.* **2013**, *13*, 2541.
- [8] V. W. Brar, M. S. Jang, M. Sherrott, S. Kim, J. J. Lopez, L. B. Kim, M. Choi, H. Atwater, *Nano Lett.* **2014**, *14*, 3876.
- [9] V. W. Brar, M. C. Sherrott, M. S. Jang, S. Kim, L. Kim, M. Choi, L. A. Sweatlock, H. A. Atwater, *Nat. Commun.* **2015**, *6*, 7032.
- [10] H. Yan, T. Low, W. Zhu, Y. Wu, M. Freitag, X. Li, F. Guinea, P. Avouris, F. Xia, *Nat. Photonics* **2013**, *7*, 394.
- [11] H. Yan, X. Li, B. Chandra, G. Tulevski, Y. Wu, M. Freitag, W. Zhu, P. Avouris, F. Xia, *Nat. Nanotechnol.* **2012**, *7*, 330.
- [12] L. Ju, B. Geng, J. Horng, C. Girit, M. Martin, Z. Hao, H. A. Bechtel, X. Liang, A. Zettl, Y. R. Shen, *Nat. Nanotechnol.* **2011**, *6*, 630.
- [13] S. Allen Jr., D. Tsui, R. Logan, *Phys. Rev. Lett.* **1977**, *38*, 980.
- [14] J.-H. Chen, C. Jang, S. Xiao, M. Ishigami, M. S. Fuhrer, *Nat. Nanotechnol.* **2008**, *3*, 206.
- [15] a) E. Hwang, S. D. Sarma, *Phys. Rev. B* **2013**, *87*, 115432; b) N. Mori, T. Ando, *Phys. Rev. B* **1989**, *40*, 6175.
- [16] M. Fox, Oxford University Press, Vol. 3, *Optical Properties of Solids*, Oxford, UK **2010**.
- [17] P. A. D. Goncalves, N. Peres, *World Scientific Publishing Co. Pte. Ltd.* **2016**.
- [18] R. Fuchs, K. Klier, *Phys. Rev.* **1965**, *140*, A2076.
- [19] N. W. Ashcroft, *Solid State Physics*, Saunders College, Philadelphia, PA, USA **1976**, p. 120.

- [20] W. Zhu, T. Low, V. Perebeinos, A. A. Bol, Y. Zhu, H. Yan, J. Tersoff, P. Avouris, *Nano Lett.* **2012**, 12, 3431.
- [21] J. Schiefele, J. Pedrós, F. Sols, F. Calle, F. Guinea, *Phys. Rev. Lett.* **2013**, 111, 237405.
- [22] a) T. Taubner, D. Korobkin, Y. Urzhumov, G. Shvets, R. Hillenbrand, *Science* **2006**, 313, 1595; b) R. Koch, S. Fryska, M. Ostler, M. Endlich, F. Speck, T. Hänsel, J. Schaefer, T. Seyller, *Phys. Rev. Lett.* **2016**, 116, 106802.
- [23] C. R. Gubbin, F. Martini, A. Politi, S. A. Maier, S. De Liberato, *Phys. Rev. Lett.* **2016**, 116, 246402.
- [24] J. A. Schuller, T. Taubner, M. L. Brongersma, *Nat. Photon.* **2009**, 3, 658.
- [25] B. Schwarz, P. Reininger, D. Ristanić, H. Detz, A. M. Andrews, W. Schrenk, G. Strasser, *Nat. Commun.* **2014**, 5, 4085.
- [26] H. Hu, X. Yang, F. Zhai, D. Hu, R. Liu, K. Liu, Z. Sun, Q. Dai, *Nat. Commun.* **2016**, 7, 12334.